Article

Particle Size Distribution and Its Impacts on Ash Deposition and Radiative Transfer during Oxy-Combustion of Rice Husk–Natural Gas

Gautham Krishnamoorthy [ID]

Department of Chemical Engineering, UPSON II Room 365, 241 Centennial Drive, University of North Dakota, Grand Forks, ND 58202-7101, USA; gautham.krishnamoorthy@und.edu; Tel.: +1(701)-777-6699

Abstract: Rice husk (RH) co-combustion with natural gas in highly oxygen-enriched concentrations presents a net carbon-negative energy production opportunity while minimizing flue gas recycling. However, recent experiments have shown enhanced ash deposition rates in oxygen-enriched conditions, with deposition/shedding also being dependent on the particle size distribution (PSD) of the parent RH fuel. To uncover the causative mechanisms behind these observations, add-on models for ash deposition/shedding and radiative properties were employed in computational fluid dynamics simulations. The combustion scenarios investigated encompassed two types of RH (US RH, Chinese RH) with widely varying ash contents (by % mass) and inlet fuel PSD with air and O_2/CO_2 (70/30 vol %, OXY70) as oxidizers. Utilizing the measured fly-ash PSDs near the deposit surface and modeling the particle viscosity accurately, particle kinetic-energy (PKE)-based capture and shedding criteria were identified as the keys to accurate deposition/shedding rate predictions. The OXY70 scenarios showed higher ash-capturing propensies due to their lower PKE. Conversely, higher erosion rates were predicted in the AIR firing scenarios. In addition, the radiative characteristics across all the scenarios were dominated by the gases and were not sensitive to the fly-ash PSD. Therefore, the higher particle concentrations in the OXY70 conditions did not negatively impact the heat extraction.

Keywords: CFD; oxy-combustion; ash deposition; shedding; co-firing

1. Introduction

Co-firing rice husk (RH) and natural gas with carbon capture using oxy-combustion presents a net carbon-negative energy production opportunity. Second-generation atmospheric-pressure oxy-combustion systems use an oxidizer stream that is highly enriched in oxygen (often > 50% O_2 by volume, OXY50) aimed at minimizing the volumetric flow rate of flue gas flowing through the combustor (as a recycle), thereby potentially improving efficiency. However, RH has a heating value comparable to that of lignite, a high ash content ($13-29$ wt. %) and is rich in silica (87–97 wt. %), which can present operational challenges resulting from the higher gas temperatures and lower gas velocities present in these novel combustion scenarios. This has been confirmed by Wu et al. [1] who showed a significant increase in ash deposition rates during RH–natural gas combustion when using a highly oxygen-enriched oxidizer stream (up to 70% O_2 by volume, OXY70). This was attributed to the formation of coarser fly-ash particles in the OXY70 scenario (resulting from a more intense combustion, higher temperatures and an increase in particle concentrations/interactions) that increased the impaction and capture efficiencies. Further, when two types of RH (US RH, Chinese RH) with widely varying ash content (by % mass) and inlet fuel PSD were fired, they showed widely varying outer deposition rates, with the coarser fuel PSD showing lower deposition and higher shedding rates [2]. Since the fly-ash PSD is dependent on the fuel PSD, the lower rebounding (and therefore higher capture) probabilities associated with fly-ash particles having a smaller particle kinetic

energy (PKE) value and the higher erosion/shedding tendencies associated with particles with a larger PKE were hypothesized as factors influencing the deposition rates. While the particle PKE plays a crucial role in outer ash deposition rates, inner ash deposition rates were also found to increase as a result of increases in sub-micron aerosol formation under OXY70 conditions [3]. However, Wu et al. [1] only employed a plug flow assumption to estimate their fly-ash impaction and capture efficiencies and explain their measurements. A more rigorous analysis that resolves the complicated flow field near the probe and takes the fly-ash mass % and compositional variations between the two RHs into account is therefore warranted to optimize operating conditions and scale-up.

Therefore, our effort here was to complement the study of Wu et al. [1] by using computational fluid dynamics (CFD) simulations where the 3D flow field near the deposit probe is well resolved to model the outer ash deposition rates. An adequate match with the measurements/trends would help to confirm Wu et al.'s [1] hypothesis that the deposition rate variations between the AIR and OXY70 scenarios were primarily due to PKE variations. Once the RH fly-ash impaction is accurately represented by employing a well resolved boundary layer in the CFD simulations, an appropriate modeling methodology for particle capture needs to be adopted. The capture or deposition of a RH fly-ash particle following impaction may be modeled based on its critical melt fraction (which is estimated from its composition-dependent equilibrium calculations), a PKE-critical viscosity-based criterion (where a calculation of a composition-dependent particle viscosity, μ_P, is necessary) or a critical-velocity- and energy-conservation-based criterion (where the angle of impaction along with additional parameters such as Young's modulus and Poisson's ratio are employed) [4]. Among these, we also hypothesized that the PKE-critical viscosity-based criterion would provide an adequate representation of the measured deposition rates/trends as long as an appropriate model for μ_P is identified and employed.

In addition to its influence on ash deposition rates, the fly-ash PSD also plays an important role in radiative transfer and heat extraction characteristics within a combustor. For instance, lower emissions and reduced heat transfer rates may be expected when coarser biomass particles are present as a result of a reduction in the particle surface area [5]. In fact, simulations of a non-swirling, oxy-coal flame in the furnace investigated in this study indeed showed that particles contributed significantly to radiative transfer in the radiant section [6]. Radiative transfer also governs the gas temperature distribution within the combustor, which affects the fly-ash temperature, its viscosity and its deposition characteristics. Therefore, in our attempts to minimize the deposition rates by changing the operating conditions to attain a favorable fly-ash PSD, we also needed to ensure that the incident heat transfer rates and heat extraction profiles were not negatively impacted. In addition to the PSD, the particle and gas radiative properties and the scale of the combustor all play an important role on the overall heat extraction rates, as summarized in Table 1.

Table 1. A summary of previous studies assessing the relative importance of gas and particle radiation in oxy-combustion scenarios.

Reference	Summary
K. Andersson et al. [7]	OXY 25–29 scenarios were investigated in a 100 kW furnace. A large fraction of the radiation was emitted by particles (assumed to be soot). An increase in the CO_2 concentration in the OXY scenarios did not impact the radiative fluxes if the temperature was identical to combustion in air. A wavelength-dependent complex index of refraction was employed for soot, and its volume fraction was modeled (not measured).
G. Krishnamoorthy et al. [8]	Dry- and wet-recycle scenarios were investigated at lab- and full-scale (300 MW) geometries. Particle radiation dominated at small scales, and inaccuracies in the gas radiation modeling did not impact the predictions at this scale. Fuel-conversion-dependent particle radiative properties were employed. However, gas radiation became more important at larger scales, thereby requiring the use of accurate emissivity models corresponding to the H_2O/CO_2 ratios within the boiler.
P. Nakod et al. [9]	Dry- and wet-recycle scenarios were investigated at lab- and full-scale (300 MW) geometries. Particle radiation dominated at small scales, and no differences were found when employing either a gray or non-gray radiation model for the gas phase. However, gas radiation became more important at larger scales, and employing an accurate non-gray model for gas radiative properties was deemed necessary. Particle radiative properties were modeled based on fuel conversion.
G. Krishnamoorthy and C. Wolf [10]	Simulations of air and oxy-combustion of coal/biomass blends in a 0.5 MW combustion test facility were carried out. Accounting for the fuel-conversion-dependent particle radiative property variations was determined to be important as opposed to employing constant particle radiative properties. The lower gas flow rates through the furnace during oxy-combustion resulted in higher particle concentrations and particle extinction coefficients when compared against combustion in air. The resolution of the particle PSD and changes to PSD due to particle swelling had an impact on the incident radiative fluxes. Isotropic and forward scattering phase functions resulted in identical radiative fluxes.
J. Zhang et al. [11]	Simulations of a prototypical furnace as well as a front-wall-fired 100 MW boiler were carried out. Contrary to a previous study [9], the wall radiative fluxes in the boiler were relatively insensitive with either the gray or non-gray gas property model. This suggested that the particle temperature could be employed to calculate the non-gray weighting factors for particle emission.
X. Yang et al. [12]	In a small-scale furnace (250 kW), both gas and particle radiation were deemed to be important. A higher particle emission was predicted when employing constant radiative properties. However, gas radiation dominated at larger scales (35 MW). The scattering efficiencies were in the range 0.1–0.4 based on the Mie theory.
B.R. Adams and T.R. Hosler [13]	Smaller ash particles, by virtue of their higher concentrations, could increase the scattering and heat fluxes. Forward scattering was a reasonable first approximation, but the phase function became more important at smaller sizes. An accurate representation of the particle size distribution was important in calculating the absorption and scattering coefficients. However, a Sauter mean diameter could be used with reasonable accuracy for radiation calculations if a single particle size must be used to represent a poly-disperse particle distribution.
V. Kez et al. [14]	Radiative transfer calculations were carried out in a prototypical 2D geometry representative of wet oxy-combustion. Temperature, specie, coal and ash concentration profiles were represented as functional forms. Particle radiation accounted for 50% of the radiative transfer. The choice of the complex refractive index for ash particles strongly impacted the results.
J. Guo et al. [15]	In a 2.5 MW furnace, radiation in the flame zone was dominated by particle contributions, whereas the burnout region was dominated by gas. Particle property variation with burnout was important, otherwise the particle radiation was over-estimated during oxy-fuel combustion.

It is important to note that the studies listed in Table 1 were primarily concerned with first-generation oxy-combustion systems, where the maximum O_2 concentration in the oxidizer stream was 30% O_2 by volume (OXY30). In addition, while the majority of the studies highlight the importance of fly-ash radiation characteristics, none of the studies employed a measured fly-ash PSD to assess the radiation impacts. For instance, Johansson et al. [16] highlighted the importance of fly-ash PSD as the most important

parameter compared to any of the uncertainties in the fly-ash complex index of refraction in the radiation calculations while emphasizing that an appropriate Sauter mean diameter may be used for radiation calculations without significant losses in accuracy, which aligned with the conclusions of Adams and Hosler [13].

In summary, in order to understand the effects of the PSD on the deposition and radiative transfer processes in second-generation oxy-combustion systems, we sought answers to the following questions in this study:

1. Can the effects of fly-ash PKE on the measured deposition/shedding rates be modeled based on available data? Since the OXY70 scenarios investigated by Wu et al. [1] and Wang et al. [2] were associated with a three-fold reduction in volumetric flow rates in comparison to the AIR scenario, the implications of this may extend beyond designing second-generation oxy-combustion systems to optimizing load-following operations involving biomass firing that are also associated with a significant (60–70%) reduction in combustor flue gas flow rates when compared to baseload operation.

2. Can a PKE-critical viscosity-based criterion be employed to model the capture/deposition of RH fly-ash given the widespread variability in its composition and properties [17]? While recent efforts have focused on predicting deposition propensities based on an equilibrium-based approach that uses fly-ash compositions and temperature to estimate the melt fractions and liquidus temperatures of the fly-ash [1,18], the potential for using a PKE-critical viscosity criterion for biomass fly-ashes has been shown by Schulze et al. [19]. During this process, we also attempted to identify an appropriate model for the particle viscosity, μ_P, in our calculations.

3. Given our current lack of knowledge regarding the relative importance of gas and particle radiation in second-generation atmospheric pressure oxy-combustion systems (cf. Table 1), we also wanted to quantify the contribution of fly-ash on the radiative transfer processes given that its concentrations would be higher at these greatly reduced flue gas volumetric flow rates. In addition to the higher particle concentrations, the generation of coarser fly-ash particles (in comparison to firing in air) may further magnify its radiation contribution.

2. Results and Discussion

2.1. Carbon Burnout

Figure 1 shows the regions of carbon burnout in the four simulation scenarios when employing the shrinking core heterogeneous combustion methodology. In spite of the wide variation in the particle PSD of the parent fuels [cf. Figure 2a,c], complete char burnout was accomplished in the ignition zone [cf. Figure 3] well upstream of the deposit probe. Since no unburnt carbon was noted in the probe ash deposits in the experiments [2], this provided a preliminary confirmation regarding the adequacy of the combustion models employed in the simulations (cf. Table 2). However, a slightly earlier onset of burnout prediction (closer to the burner) was noted in the OXY70 scenarios as a result of increased thermal (higher temperatures) and mass diffusion (higher O_2 concentrations).

Table 2. Physics-based models employed in this study.

Physics Being Modeled	Modeling Option
Particle devolatilization (heterogeneous)	Constant rate (50, 1/s)
Char oxidation (heterogeneous)	Kinetic/diffusion-limited: shrinking core (PSD remains unchanged from that of parent fuel), shrinking sphere * (density fixed at 1700 kg/m^3 and PSD varies depending on mass consumption)
Volatile combustion (homogeneous) to form products: CO, H_2O, N_2, SO_2	Finite rate/eddy dissipation
CO oxidation to form CO_2 (homogeneous)	Finite rate/eddy dissipation
Turbulence	Realizable k-epsilon
Particle drag law	Morsi–Alexander
Model describing radiative transport	Discrete ordinates
Particle radiative property	Particle-burnout-dependent absorption (Q_{abs}) and scattering efficiencies (Q_{scat}) [10] *
Particle scattering phase function	Anisotropic (forward scattering)
Gas-phase radiative property	Non-gray weighted sum of gray gases [20] *
Ash capture/deposition	Particle-kinetic-energy-critical viscosity-based criterion [21] *
Ash shedding	Particle-kinetic-energy-based criterion *

* These models were implemented as user-defined functions or add-on modules.

2.2. Gas Temperature

Figure 4 shows the centerline gas temperature predictions with corresponding measurements from Wang et al. [2]. A good agreement between the predictions and measurements was observed across all the scenarios. The agreement in the vicinity of the deposit probe, where the gas temperatures were around 1250–1300 K, is particularly noteworthy. While the profiles in Figure 4 correspond to those obtained from the shrinking core heterogeneous combustion model, the profiles from the shrinking sphere model did not result in any discernible differences between the temperature profiles and are not shown here for brevity.

2.3. Radiant Fractions

Having ascertained that the combustion characteristics and gas temperatures within the combustor were being adequately represented, the individual contributions of gas and particles to the overall radiative transfer were assessed next. For this, a radiative fraction was defined as the ratio of the total net radiative fluxes transferred to the walls of the combustor to the total thermal input (fuel flow rate × heating value). Table 3 reports the percentage radiative fraction computed across all four scenarios when employing the shrinking core heterogeneous combustion model. Surprisingly, in spite of the strong dependency of the particle absorption and scattering coefficients on the PSD (cf. Equations (1) and (2)), the radiative fractions did not change between the shrinking core and shrinking sphere simulation scenarios. Further, even when the effects of particle radiation were completely ignored by setting the particle absorption and scattering efficiencies to zero, the changes to the radiative fraction reported in Table 3 were minimal. This indicated that the radiation in the investigated scenarios was dominated by the participating gases. Further, the radiative fraction was noted to be higher in the OXY70 scenario due to the higher temperatures near the burner (cf. Figure 4) and the higher concentrations of CO_2 and H_2O within the combustor.
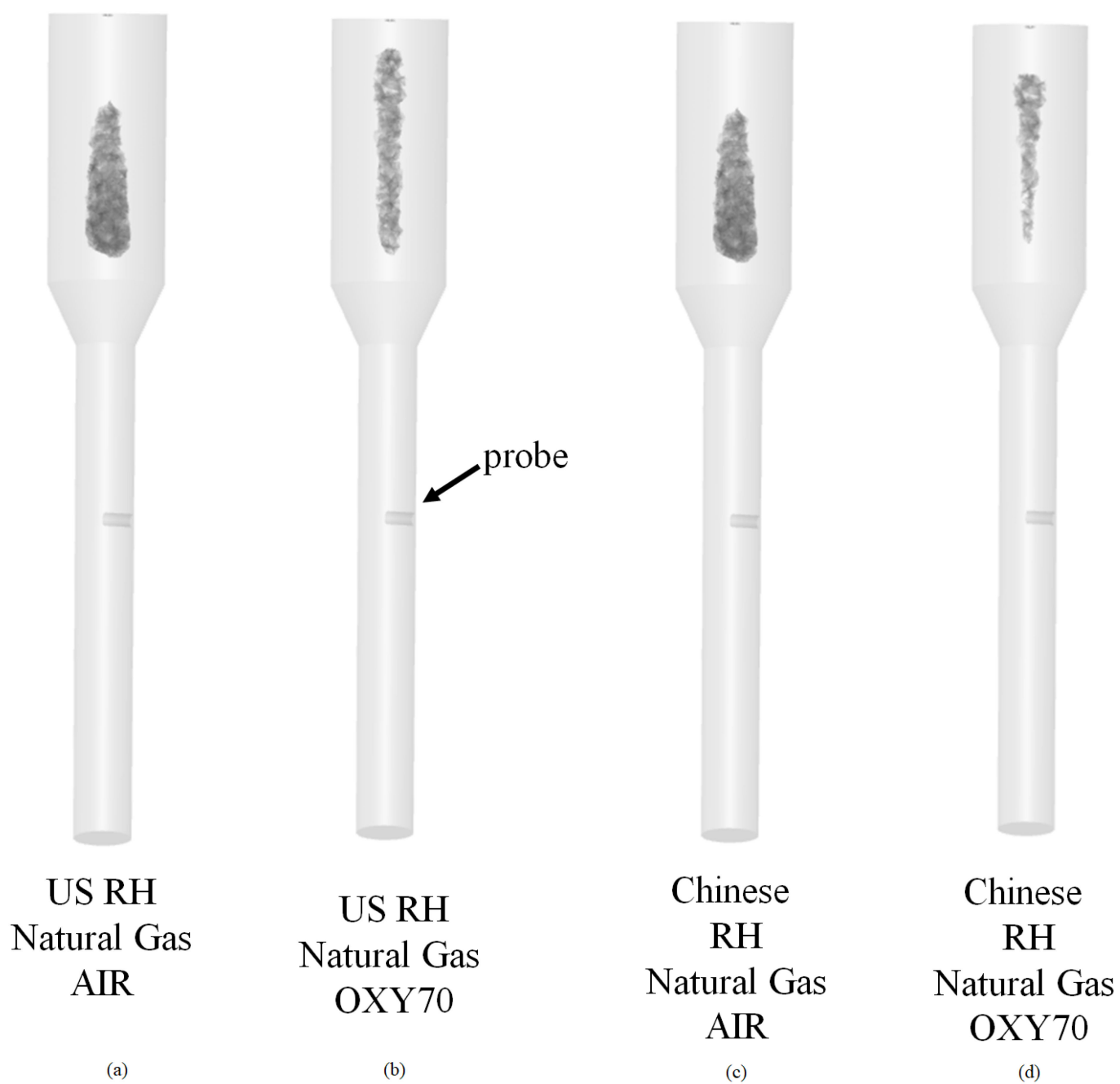
Figure 1. Regions of carbon burnout. Complete carbon burnout was predicted in the ignition zone (wide section) before reaching the probe (indicated by arrow).
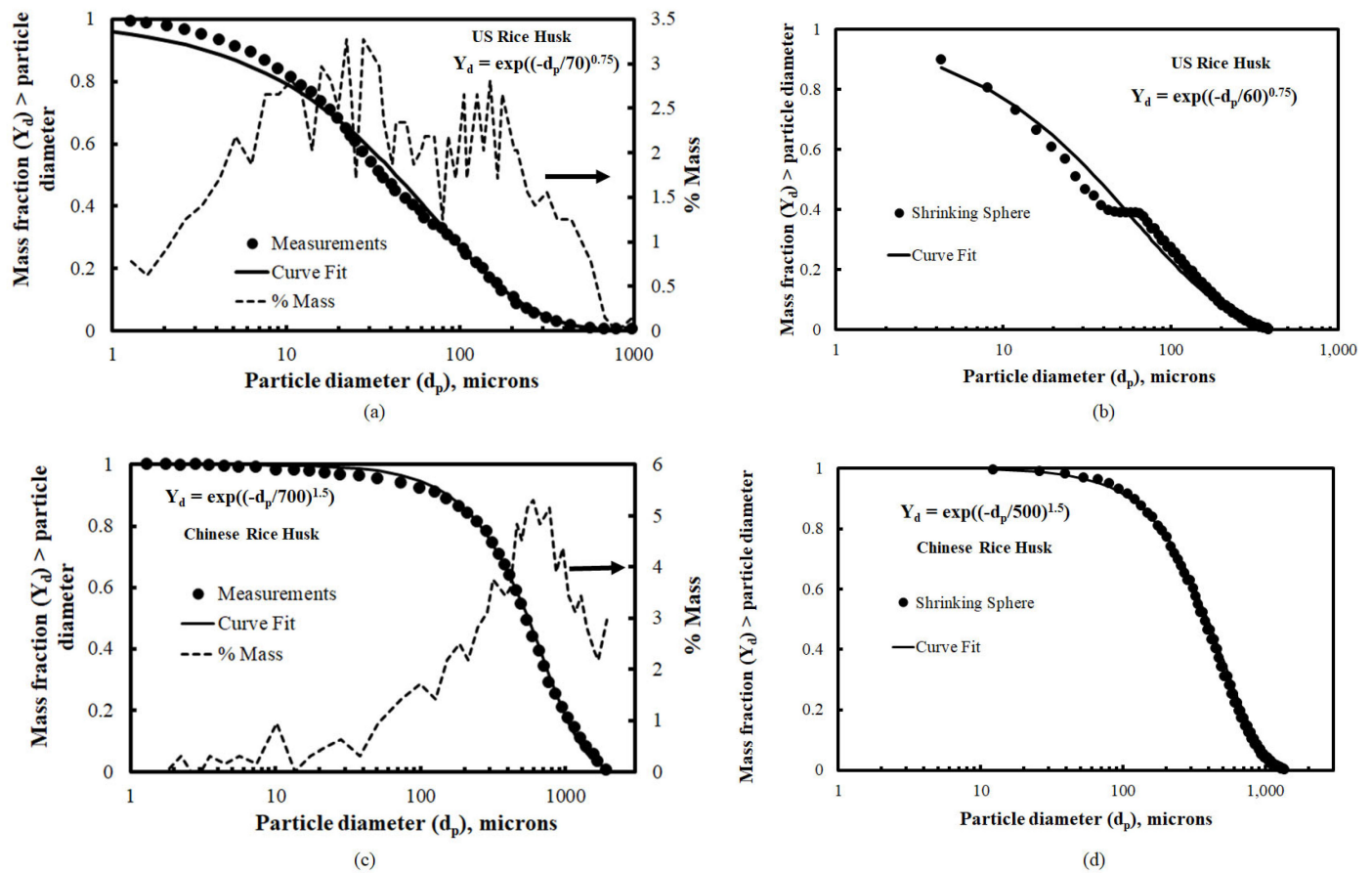
Figure 2. The measured and modeled particle size distributions (PSDs) of the parent fuel: (**a**) US RH (shrinking core); (**b**) US RH (shrinking sphere); (**c**) Chinese RH (shrinking core); (**d**) Chinese RH (shrinking sphere).

Table 3. Predicted % radiative fractions.

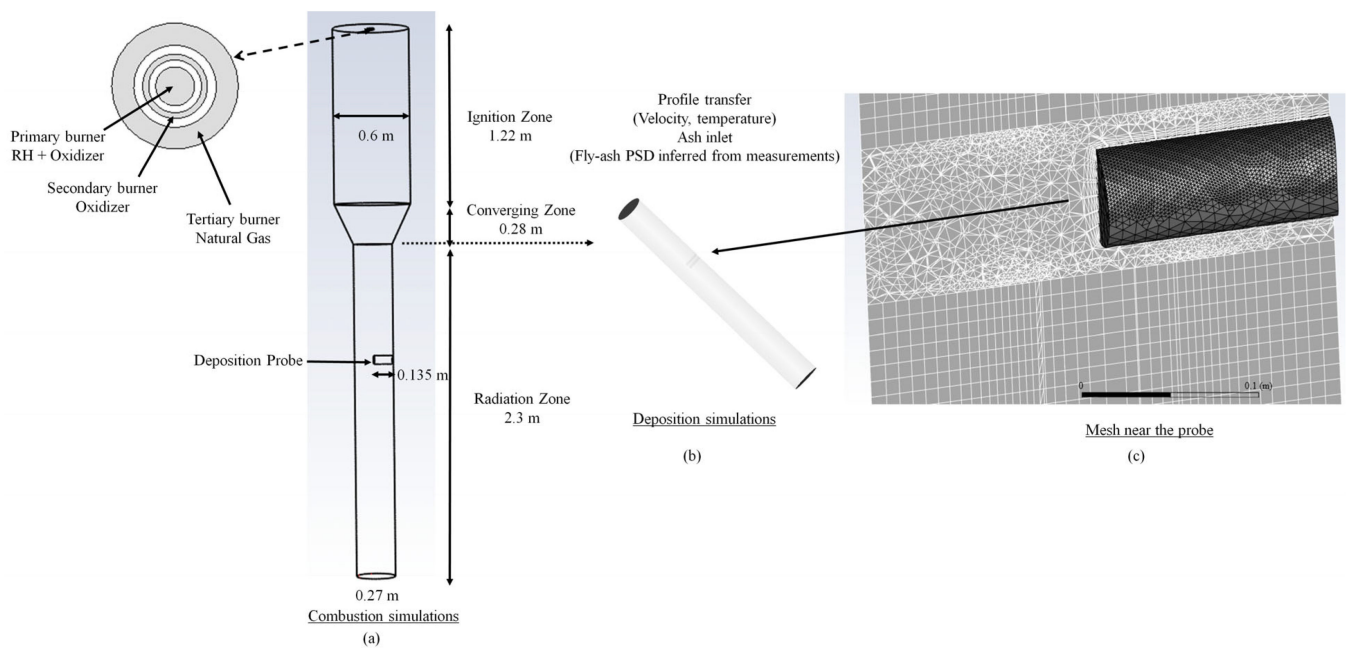|	Radiative Fraction (Gas + Particle)	Radiative Fraction Gas Only (Without Particle Radiation)
US RH AIR	81	80
Chinese RH AIR	83	82
US RH OXY70	95	95
Chinese RH OXY70	95	95

Figure 3. Geometric details of the down-flow OFC combustor. (**a**) Domain for combustion simulations; (**b**) domain (radiation zone only) for the ash deposition simulations where the measured fly-ash PSD and density were employed to model the deposition rates; (**c**) the finely resolved mesh near the probe.

2.4. Ash Deposition Rates Using Shrinking Core and Shrinking Sphere Methodologies

Table 4 shows the impaction and deposition rates when employing the shrinking core and shrinking sphere methodologies. First, it is noteworthy that the impaction rates did not vary significantly between the two methodologies in spite of the fly-ash PSD variations between the two models (cf. Figure 2). Second, since the impaction rates were solely a function of particle Stokes number (*Stk*), it is surprising that the OXY70 scenarios (where the particle velocities and therefore the Stokes number were lower) showed a higher impaction rate than the corresponding AIR scenario. Stk is defined as:

$$Stk = \frac{\rho_p {d_p}^2 u_p}{9 \mu_g d_c} \tag{1}$$

Table 4. Impaction and deposition rates employing shrinking core/shrinking sphere methodologies.

Units: g/m²-h	Measured Deposition Rates	Predicted Deposition Rates (Shrinking Core)	Predicted Deposition Rates (Shrinking Sphere)	Predicted Impaction Rates (Shrinking Core) ($\eta^{impaction}$)	Predicted Impaction Rates (Shrinking Sphere) ($\eta^{impaction}$)
US RH AIR	160 ± 70	0	0	250 (16)	307 (19)
US RH OXY70	220	13	17	475 (30)	484 (30)
CH RH AIR	30 *	1	1	489 (68)	466 (65)
CH RH OXY70	160 *	1	2	542 (75)	600 (83)

* Measured deposition rates averaged across the first 20 min prior to shedding onset.
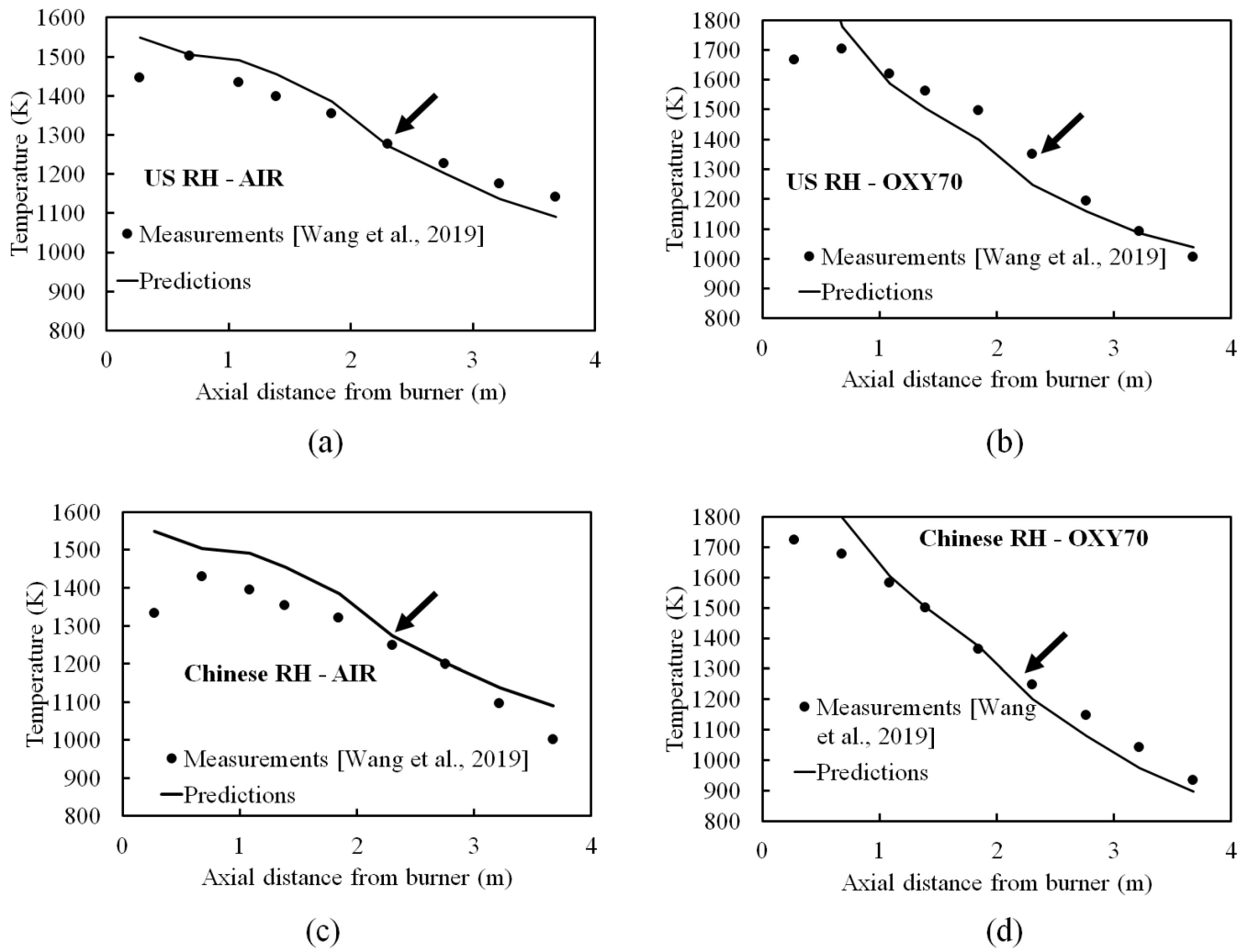
Figure 4. Comparison of centerline temperature predictions against measurements [2] along the axial length of the combustor (**a**–**d**).

In Equation (11), u_p is the average particle velocity near the probe, d_p is the particle diameter, ρ_p is the particle density, μ_p is the gas viscosity and the probe diameter, $d_{c,}$ is equal to 0.06 m.

Impaction efficiencies ($\eta^{impaction}$) were defined as:

$$\eta^{impaction} = \frac{m_{impact} A_p}{m_f x_f A_c}$$

(2)

where m_{impact} is the mass of ash impacting the probe, m_f is the mass of fuel fed into the furnace, x_f is the ash content of the fuel, A_c is the projected area of the probe and A_p is the cross-sectional area of the OFC. Wu et al. [1] estimated the $\eta^{impaction}$ of the Chinese RH to be around 35% for both the AIR and OXY70 scenarios by performing plug flow calculations, employing the fly-ash PSD. The ash deposition rates on the probe were monitored, and the corresponding collection efficiencies ($\eta^{impaction}$) were defined as:

$$\eta^{collection} = \frac{m_d A_p}{m_f x_f A_c}$$

(3)

Note that capture and erosion efficiencies were estimated from the predicted $\eta^{impaction}$ and $\eta^{collection}$ as follows:

$$\eta^{capture} = \frac{\eta^{collection}}{\eta^{impaction}} \tag{4}$$

Since the fly-ash PSDs following complete burnout remained identical between the AIR and OXY70 scenarios, this points to complex flow features near the deposit probe where the local segregation of particles may occur where larger-sized particles were likely impacting the probe in the OXY70 scenarios and flowing around the probe in the AIR scenarios. Similar observations were made by Krishnamoorthy et al. [22] in OXY27 and OXY70 scenarios where the fly-ash PSD values were identical to the parent fuel PSD (shrinking core), yielding identical impaction rates in spite of a 2.5-fold variation in the volumetric flow rates. In addition, the predicted deposition rates using both the shrinking sphere and shrinking core methodologies were significantly lower than the measured deposition rates. This can be reconciled based on the PKE of the impacting particles, as shown in Figure 5. It is noteworthy that the majority of the particles across all the scenarios had a PKE > 1×10^{-10} J. In addition, the fly-ash viscosities were $\mu_P > 10^6$ Pa-s at a temperature of 1250 K. Particles that meet both these criteria were likely to "bounce off" as per our capture criterion (cf. Figure 6b). Therefore, the PKE distribution likely needs to be much lower than those predicted from either the shrinking core or shrinking sphere modeling options to match the measured deposition rates. Therefore, this indicated that a well-characterized fuel PSD by itself was insufficient to match the deposition rates/trends, pointing to a need for more accurate fly-ash PKE distributions near the probe prior to impact. In addition, to obtain an accurate resolution of the gas velocities near the probe, a knowledge of a reasonable fly-ash PSD in conjunction with fly-ash densities would be required.

2.5. Ash Deposition Rate Predictions from Measured Fly-Ash PSD

Since fly-ash PSD and densities cannot be tailored/controlled simultaneously when employing heterogeneous combustion methodologies such as the shrinking core/shrinking sphere methods, a decoupled approach was required, where fly-ash of a specified PSD (either measured or reasonably approximated) and fixed density (estimated as 1700 kg/m³ in this study) were injected as inert particles from a section where complete burnout had been accomplished (cf. Figure 3b). In addition, the velocity, temperature and species profiles from the fully coupled simulations were also transferred. Since this region of the domain was only associated with the cooling of the flue gas (following complete combustion), this was a reasonable approach, the validity of which has been demonstrated by us previously [21,26]. Fortunately, measurements of the fly-ash PSD near the deposition probe for the Chinese RH were available from Wu et al. [1] and are shown in Figure 7. The measurements were fit using a Rosin–Rammler functional form and are also shown in Figure 7 and were simulated using 100 discrete bins. It is worth noting that OXY70 resulted in a coarser fly-ash PSD (a mean diameter of 100 μm as opposed to the mean diameter of 70 μm resulting from combustion in the AIR scenario) due to the higher temperatures and longer residence time within the combustor. The impaction and deposition rate predictions when using the measured fly-ash PSD in a decoupled manner as shown in Figure 3b are reported in Table 5. First, unlike the observations in Table 4, where higher impaction rates were associated with the OXY70 scenario, the impaction rates were identical between the AIR and OXY70 scenarios when the measured fly-ash PSD and correct ash densities (1700 kg/m³) were employed in the simulations. This was attributed to increased agglomeration and coarser particles, resulting in the OXY70 scenario that yielded fly-ash Stokes numbers similar to those observed in the AIR scenario in spite of a 60–70% reduction in gas velocities. However, we caution that the impaction rate differences between the two scenarios (AIR and OXY70) were very specific to the fly-ash PSD. For instance, when employing measured coal fly-ash PSD in decoupled calculations, we indeed showed 2.5–3.7 times higher impaction rates in the OXY70 scenarios [21,26].
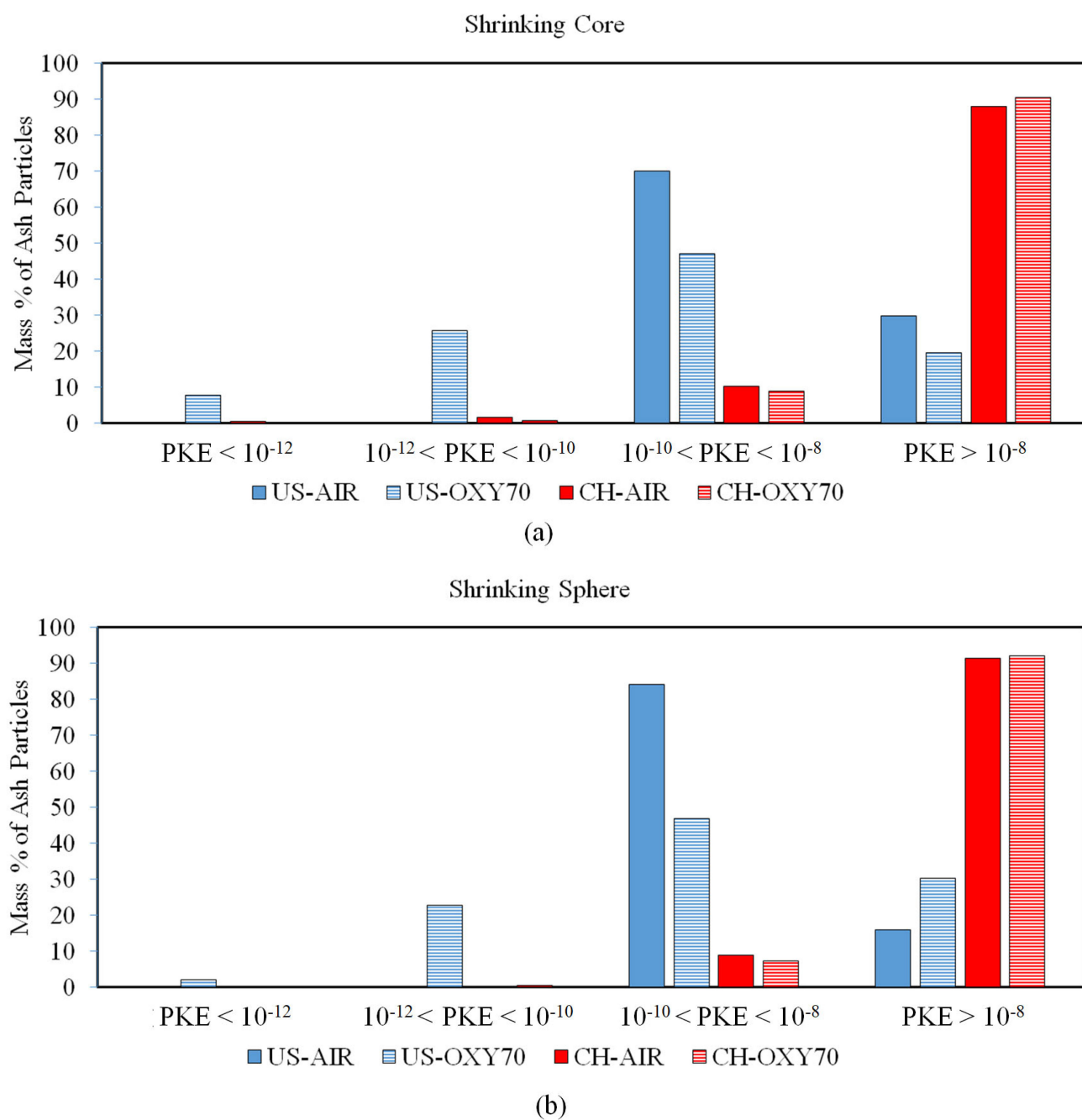
Figure 5. Particle kinetic energies (in J) using different modeling methodologies: (**a**) shrinking core; (**b**) shrinking sphere.

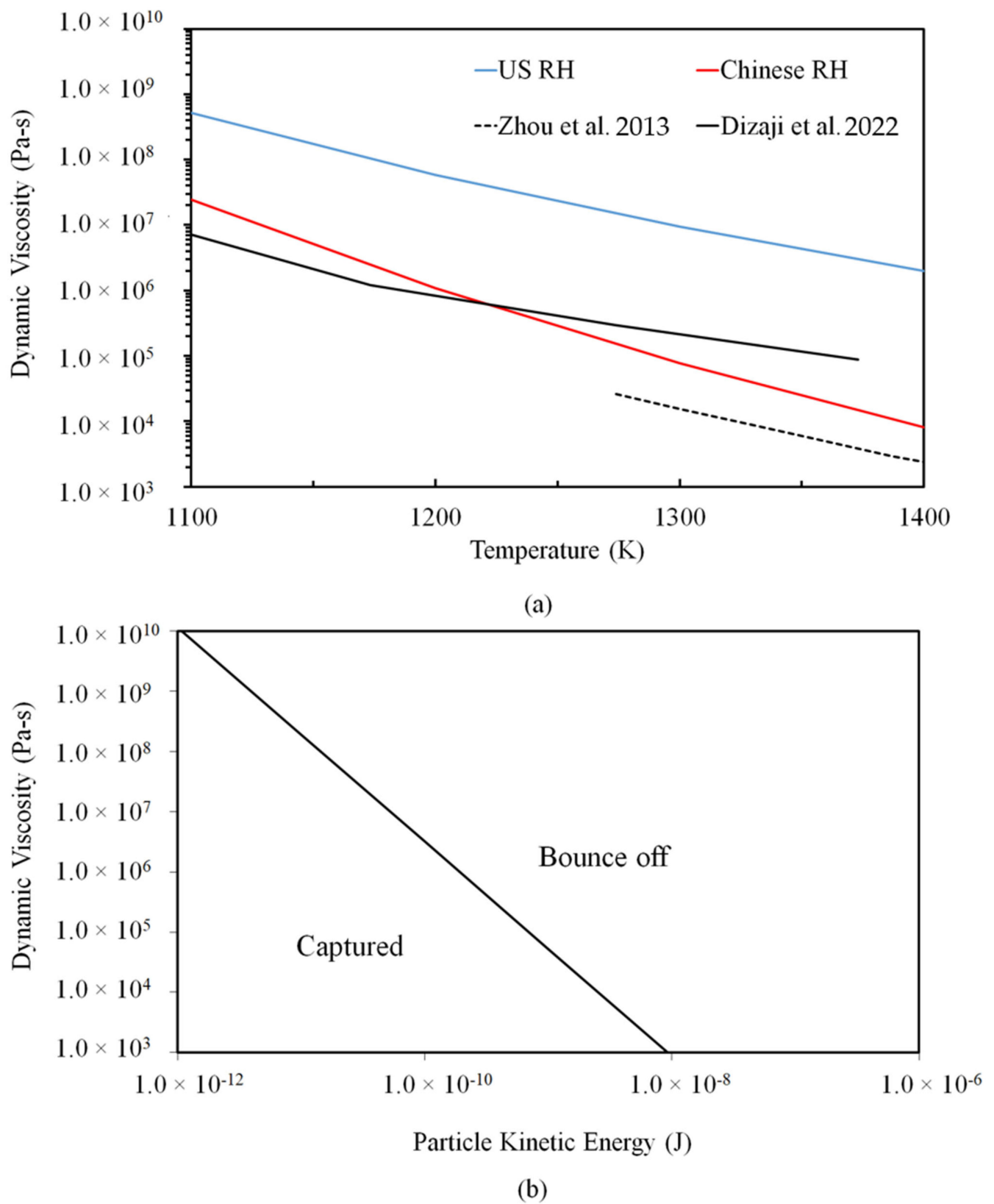**Figure 6.** (**a**) RH ash viscosity predictions employing different models from Senior and Srinivasachar [23–25] (Equation (5)); (**b**) the sticking criterion (Equations (3) and (4)) represented as a function of particle viscosity (μ_P) and particle kinetic energy (PKE).

Second, Table 5 shows that the deposition rates were more in line with the measured values, indicating an improved estimate of fly-ash PKE distributions in these scenarios, as shown in Figure 8. The capture efficiencies were marginally higher in the OXY70 scenario due to the lower PKE. Conversely, the higher PKE in the AIR scenario resulted in higher erosion rates. The differences in the deposition rates reported in Tables 4 and 5 may be explained by comparing the PKE distributions in Figures 5 and 8. The shrinking core and shrinking sphere methodologies, even when based on well-characterized fuel PSD information, tended to over-estimate the PKE (cf. Figure 5), causing more particles to rebound as per our capture criterion (cf. Figure 6b). However, when a measured fly-ash PSD, in conjunction with the ash densities, was employed, the accuracies in the PKE predictions improved. Figure 8 shows that the PKE distributions shifted to lower ranges (in comparison to Figure 5), thereby enabling higher capture rates and bringing our deposition rate predictions in line with the measured values.

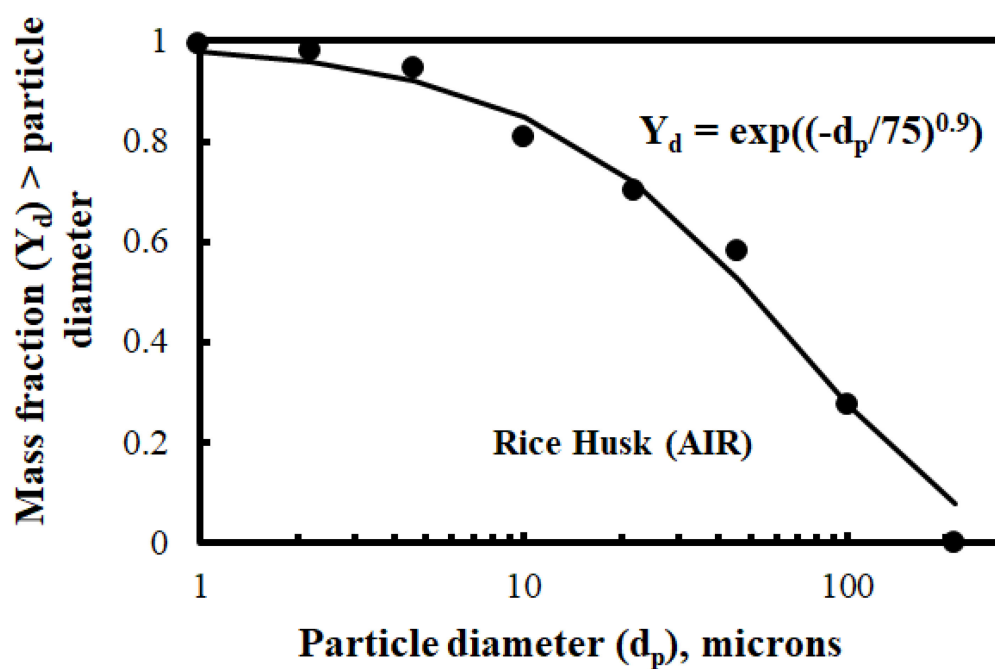**Table 5.** Predicted impaction, deposition and erosion rates for Chinese RH.

Units: g/m²-h	Measured Deposition Rates	Predicted Impaction Rates ($\eta^{impaction}$)	Predicted Deposition Rates (Without Erosion)	Predicted Erosion Rates	Predicted Deposition Rates (With Erosion)	Predicted Capture Efficiency ($\eta^{capture}$)	Predicted Erosion Efficiency ($\eta^{erosion}$)
CH RH AIR	30 *	117 (16)	86	24	62	74	28
CH RH OXY70	160 *	124 (17)	105	12	93	85	12

* Measured deposition rates averaged across the first 20 min prior to shedding onset.
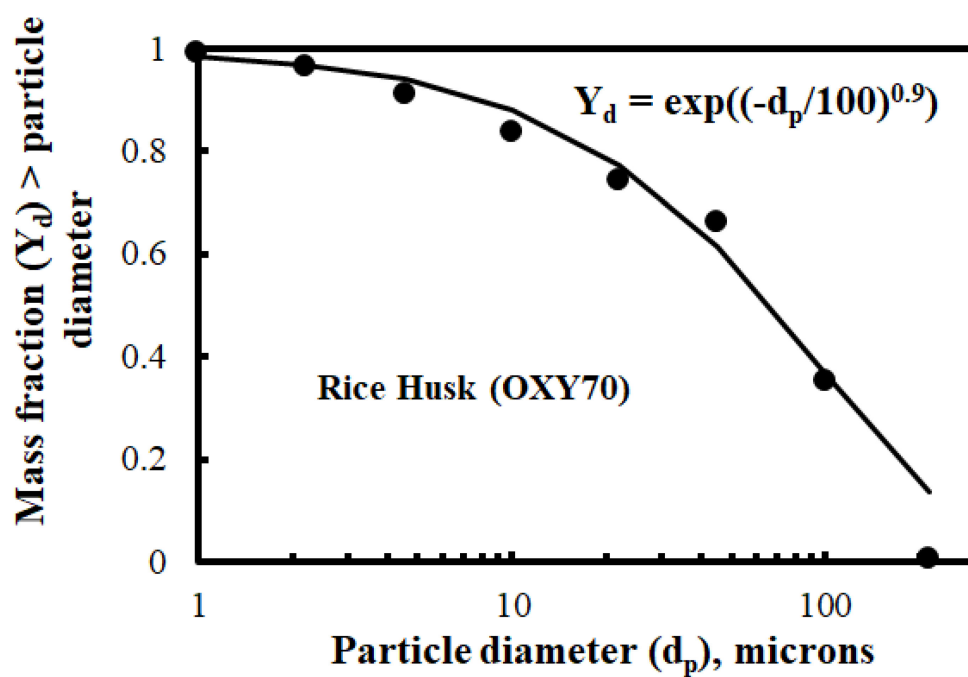
Table 6 reports the results from similar decoupled calculations based on reasonable estimates of the fly-ash PSD. Again, the impaction rates were similar between the AIR and OXY70 scenarios in spite of employing similar fly-ash PSD values in the two scenarios and the lower velocities associated with the OXY70 scenario. This indicated complex flow behavior near the probe, causing a higher particle Stk near the probe in the OXY70 scenario, a feature that cannot be captured using simple plug flow assumptions. However, higher capture rates were observed in the OXY70 scenario due to the lower PKE. Correspondingly, higher erosion rates were observed in the AIR scenario, which were attributed to the higher PKE. Further, the deposition rates were in reasonable agreement with the measured values shown in Table 4.

Table 6. Predicted impaction, deposition and erosion rates for US RH.

(Mean Diameter, Spread)	Predicted Impaction Rates g/m²-h ($\eta^{impaction}$)			Predicted Deposition Rates (Without Erosion) g/m²-h ($\eta^{capture}$)			Predicted Erosion Rates g/m²-h ($\eta^{erosion}$)		
	(35, 1.1)	(50, 1.1)	(50, 0.9)	(35, 1.1)	(50, 1.1)	(50, 0.9)	(35, 1.1)	(50, 1.1)	(50, 0.9)
US RH AIR	166 (23)	234 (15)	225 (14)	67 (41)	69 (30)	60 (26)	5 (7)	18 (25)	27 (46)
US RH OXY70	176 (25)	238 (15)	230 (14)	134 (76)	152 (64)	133 (58)	0 (0)	3 (2)	7 (5)

(a)

(b)

Figure 7. The measured (dots) and modeled particle size distribution (PSD) of the fly-ash particles near the deposit probe (shown as a bold line): (**a**) Chinese RH (AIR); (**b**) Chinese RH (OXY70).
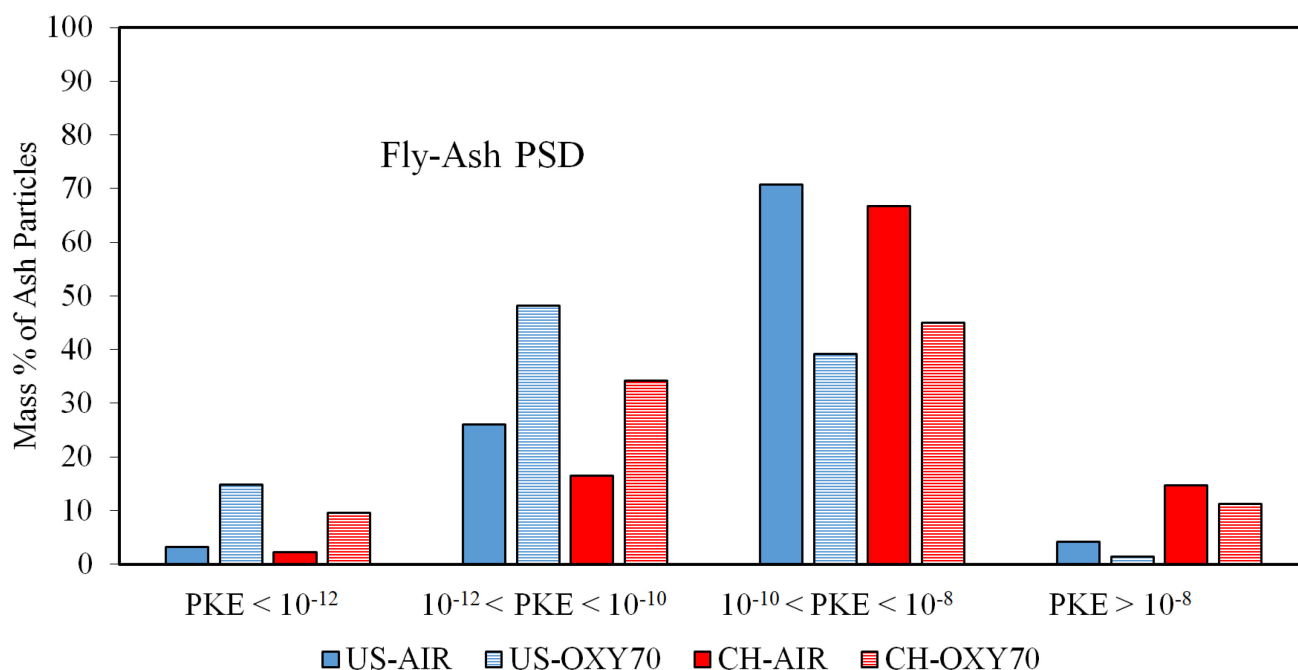
Figure 8. Particle kinetic energies (in J) using fly-ash PSD.

3. Materials and Methods

A computational fluid dynamic (CFD) methodology with add-on modules for gas radiative properties, particle radiative properties and ash deposition modeling were utilized in this study to answer the aforementioned questions.

The 3D geometry representation of the down-flow laboratory combustor (oxyfuel combustor or OFC) at the University of Utah that was employed in the investigations of Wu et al. [1] and Wang et al. [2,3] was simulated in this study and is shown in Figure 3a. The geometry was meshed with 1.1 M cells after ensuring the grid convergence of the temperature and velocity fields at this level of refinement. We also made sure that the boundary layer surrounding the ash probe was of sufficient resolution (as per the criteria set forth in Weber et al. [27]) to ensure accurate particle impaction predictions, i.e., we ensured that the size (Δ) of the numerical cells adjacent to the cylindrical probe of diameter D was well within the constraint $\Delta \leq 0.3240D/4\sqrt{Re}$. All the simulations were carried out in ANSYS FLUENT v 21 [28]. The walls of the ignition zone (cf. Figure 3a) were set to a temperature of 1250 K. The homogeneous gaseous combustion reactions were simulated using a two-step mechanism with CO being produced during devolatilization followed by its oxidation to CO_2 during the second reaction. The particle tracking was accomplished in a Lagrangian reference frame where the particle trajectory was carried out by taking into account various forces such as discrete phase inertia, hydrodynamic drag and the force of gravity.

Table 7 summarizes the proximate and ultimate analyses of the fuels simulated in this study, which were based on the experimental information reported in Wang et al. [2], and the key flow rates corresponding to the experimental scenarios that were investigated are reported in Table 8.

Table 7. Characteristics of the rice husks (RH) employed in this study.

		Proximate Analysis (wt. %)		Ultimate Analysis (wt.%, Dry Ash Free)
US RH	Fixed Carbon	9.22	C	28.47
	Volatiles	48.96	H	4.15
	Ash	33.67	N	1.05
	Moisture	8.16	S	0.1
	HHV(kJ/kg)	11551	O	24.42
Chinese RH	Fixed Carbon	13.75	C	35.78
	Volatiles	60.76	H	5.08
	Ash	15.08	N	0.44
	Moisture	10.41	S	0.082
	HHV(kJ/kg)	14576	O	33.13

Table 8. Inlet and wall boundary conditions employed in this study.

	US RH AIR	US RH OXY70	Chinese RH AIR	Chinese RH OXY70
RH mass flow rate (kg/h)	0.86	0.86	0.86	0.86
Natural gas mass flow rate (kg/h) (tertiary burner)	2.0	2.0	2.0	2.0
Primary burner oxidizer mass flow rate (kg/h)	10.8	10.8	10.8	10.8
Primary burner species concentrations (mol%)				
O_2	21	21	21	21
N_2	79	0	79	0
CO_2	0	79	0	79
Secondary burner oxidizer mass flow rate (kg/h)	30.6	7.2	30.6	7.2
Secondary burner species concentrations (mol%)				
O_2	21	100	21	100
N_2	79	0	79	0
CO_2	0	0	0	0

The different physics-based models employed to simulate the turbulent combustion process in this study are summarized in Table 2. Although the maximum y+ value at the probe resulting from the finely resolved mesh (cf. Figure 3c) was less than 1 across all the investigated scenarios, the y+ value was greater than 1 in several regions away from the probe. Consequently, the Menter–Lechner (y+ insensitive) modeling option was employed for the near-wall treatment [28].

The add-on modules utilized in this study along with the motivation for doing so are briefly summarized below:

Shrinking sphere heterogeneous combustion model: The default heterogeneous combustion modeling option in ANSYS FLUENT [28] adopts a shrinking core methodology, where the PSD of the fly-ash is the same as that of the parent fuel, and any mass loss resulting from the combustion process is accounted for by varying the particle density. For instance, Figure 2a,c show the measured [2] and modeled PSDs of the parent fuel. As per the shrinking core model, the PSD of the fly-ash exiting the combustor (following complete burnout) remains the same as the corresponding parent fuel PSD. To alleviate this shortcoming, the density of the combusting particle was fixed at 1700 kg/m^3, causing the diameter of the particle to change to account for the mass loss. We called this the "shrinking sphere" model. Figure 2c,d show the fly-ash PSD at the outlet when applying this methodology. The US RH, by virtue of its higher ash content (cf. Table 7), showed a lower percentage change in its size compared to the Chinese RH. The modeled distributions were fit to the functional form of a Rosin–Rammler distribution and are also shown in the corresponding figures and were simulated using 100 discrete bins.

Customized gas radiative property models: The OXY70 combustion scenarios were characterized by low H_2O/CO_2 ratios (<0.5) resulting from the prevailing concentrations of radiatively participating gases. Since the default emissivity models in ANSYS FLUENT [28] are tailored towards H_2O/CO_2 ratios between 0.5–2.5 (representative of hydrocarbon combustion in air), customized and validated models for gas radiative properties were necessary.

Customized particle radiative property models: Recent efforts for discerning the radiative properties of fly-ash (i.e., its absorption and scattering efficiencies) are summarized in Table 9. Since particle absorption (Q_{abs}) and scattering efficiencies (Q_{scat}) are often reported in terms of a particle size parameter ($x = \pi d/\lambda$), where d is the diameter of the particle and λ is the wavelength of light, it may be worthwhile keeping in mind that the wavelength region 1–100 μm is of interest in combustion scenarios, with the peak emission in this study occurring at approximately the 1–3 μm wavelength range. k_{abs} and k_{scat} in Table 9 refer to absorption and scattering coefficients (in m^{-1}), respectively.

The particle absorption (k_{abs}) and scattering coefficients (k_{scat}) of the particles were computed from the absorption (Q_{abs}) and scattering efficiencies (Q_{scat}) as follows:

$$k_{abs} = \sum_N Q_{abs} \frac{A_{pn}}{V} \tag{5}$$

$$k_{scat} = \sum_N Q_{scat} \frac{A_{pn}}{V} \tag{6}$$

In Equations (1) and (2), the summation is over N particles within the control volume V, and A_{pn} is the projected area of the nth particle.

PKE-critical viscosity-based ash capture criterion: A PKE-critical viscosity-based ash capture criterion that was originally developed for silica-rich soda lime glasses, but whose validity for biomass ashes has been established, was also implemented as a UDF. In this study, a critical particle-viscosity-based capture criterion was adopted, where the capture probability (P_{stick}) was equal to unity if the particle viscosity (μ_p) was lower than the critical viscosity ($\mu_{p,critical}$):

$$P_{stick} = 1 \text{ if } \mu_p \leq \mu_{p,critical} \tag{7}$$

Otherwise, P_{stick} was zero. The following relationship between PKE (neglecting its rotational component) and critical viscosity ($\mu_{p,critical}$) proposed by Kleinhans et al. [4] was adopted:

$$\mu_{p,critical} = \frac{5 \times 10^{-12}}{PKE^{1.78}} \tag{8}$$

Table 9. A summary of recent studies for discerning the radiative properties of fly-ash.

Reference	Summary
Bäckström et al. [29]	Q_{abs} of coal and ash particles of size 10 μm were approximately 1 and 0.5, respectively, in the IR region of 1–3 μm. The corresponding Q_{scat} were 1.5 at this size range but increased to as high as 4 for smaller ash particles (1 μm).
Ates et al. [30]	Five different complex index of refraction models were compared across five ash composition variations. In the IR region of 3–10 μm, Q_{abs} was between 0 and 1 across all the particles sizes between 10–200 μm. Q_{scat} values were approximately 1.5 across this size range but increased to as high as 4 for smaller ash particles (1 μm). In conditions representative of a PC fired furnace, k_{scat} was greater than k_{abs}.

Table 9. *Cont.*

Reference	Summary
Jiayu and Xiaobing [31]	At particle volume fractions that were representative of the combustion zone of boilers (~10^{-5}), Q_{abs} and Q_{scat} of the coal and fly-ash particles were estimated to be about 1.0 and 1.5, respectively, for the particle size parameters ($x = \pi d/\lambda$) of interest in this study. However, the heat fluxes seemed to be more dependent on the phase function and more significant for smaller-sized particles
Schiemann et al. [32]	Spectrally averaged emissivity of particles was reported in specific sizes. The total emissivity was shown to decrease with decreasing the particle size and increasing the temperature. A simple linear correlation between emissivity and temperature was proposed.
Pörtner et al. [33]	The total emissivity of both coal and biomass char were shown to decrease with increasing the temperature. A simple linear correlation between emissivity and temperature was proposed.
Doner et al. [34]	Absorbance characteristics of lignite coal, biomass and hard coal were investigated and reported. For Sauter mean diameters in the range of 5–10 μm, Q_{abs} and Q_{scat} values of 1.0 and 1.5, respectively, seemed to be good approximations in the IR region of interest. The study highlighted the importance of determining the k index of the complex index of refraction.

Based on the results summarized in Table 9, Q_{abs} and Q_{scat} were determined to vary during the fuel combustion process as follows (Table 10):

Table 10. RH radiative property variations employed in the simulations.

	Q_{abs}	Q_{scat}	Q_{scat}/Q_{abs}
Parent fuel	1.13	1.3	1.15
Char	0.59	1.5	2.54
Ash	0.05	1.7	34.00

The compositional and temperature dependencies of the particle viscosity (μ_p) were modeled based on the empirical relationships proposed by Senior and Srinivasachar [23] that have previously been demonstrated to be accurate for the gas temperature range of interest in this study (1150–1250 K). Briefly, the particle viscosity μ_P (Pa-s) was expressed as a function of particle temperature T_P and two composition-dependent model constants, "A" and "B", as follows:

$$\mu = AT_p \exp\left(\frac{1000B}{T_p}\right) \tag{9}$$

The model constant "B" was first calculated from the mass fractions of the different metal oxide (M_xO_y) constituents of the ash:

$$B = f(M_xO_y) \tag{10}$$

where the metal oxide (M_xO_y) compositions of the bulk ash of the parent fuel (RH) were employed to estimate the constant B. The model constant "A" was then estimated from "B" as follows:

$$A = f(B, NBO/T) \tag{11}$$

where NBO/T is the ratio of non-bridging oxygen atoms (NBO) to the tetrahedral oxygen atoms in the glassy silica network of the ash. NBO/T was determined as a function of the metal oxide (M_xO_y) compositions of the bulk ash of the parent fuel (RH). In the

Senior and Srinivasachar model [23], two sets of the constants A and B were computed corresponding to the high-temperature and low-temperature data sets employed in their formulation. Correspondingly, two sets of particle viscosities (cf. Equation (5)) were initially computed for each particle when employing this model, and the larger of the two values was assigned to μ_P. Figure 6a shows recent measurements of the viscosities of silica-rich RH ash compared against the viscosities of the US RH and Chinese RH employed in this study.

The NBO/T (cf. Equation (7)) of the US RH and Chinese RH were 0.07 and 0.13, respectively, causing significant differences in their viscosities. Nevertheless, the viscosities were in reasonable agreement with recent measurements of RH fly-ash reported in the literature [24,25].

In Figure 6b, the sticking criterion (Equations (3) and (4)), represented as a function of particle viscosity (μ_P) and particle kinetic energy (PKE), is represented as a diagonal line demarcating the sticking and rebounding conditions. The gas temperature near the deposit probe was measured to be near 1250 K [2]. This indicated that the particle viscosity (μ_P) for the RH fly-ash was in the vicinity of 10^6 and 10^8 Pa-s for the Chinese RH and US RH, respectively. Figure 6b provides a preliminary indication of the deposition propensities by suggesting that the PKE should be less than 10^{-10} and 10^{-11} J for the Chinese RH and US RH, respectively, for capture.

Erosion or shedding model: An erosion/shedding criterion was developed based on the framework provided by Zhou and Hu [35] and implemented as a UDF. The energy (*E*) required to remove the deposit was computed as follows:

$$E = 2\pi d_{dep}^2 \gamma \left(1 - \left[\sqrt[3]{1-\eta}\right]\right) \tag{12}$$

where d_{dep} is the diameter of the deposit, η is the melt fraction of the deposit, assumed to be 0.2 at 1300 K as per the equilibrium calculations of Wu et al. [1], and the surface tension, γ, was modeled as a function of the particle temperature, T_p, as follows:

$$\gamma = -0.0003T_p + 0.66 \tag{13}$$

d_{dep} was expressed as a function of the impacting particle diameter through a spreading ratio computed as follows:

$$d_{dep} = \left[\frac{4sin\theta}{Tan^2\theta(2+cos\theta)}\right]^{\frac{1}{3}} d_p \tag{14}$$

where a value of 67 degrees was assigned for θ as per Zhou and Hu [35].

4. Conclusions

Second-generation oxy-combustion systems, where rice husk (RH) is co-combusted with natural gas in highly enriched oxygen concentrations (~70 mol % in oxidizer), present a net carbon-negative energy production opportunity while minimizing flue gas recycling. In addition, by tailoring/controlling the particle size distribution (PSD) of the non-sticky (high fusion temperature), silica-rich RH fly-ash, the ash deposition could be controlled by either minimizing the particle impaction or intentionally promoting the impaction-based shedding of the deposits. However, the fly-ash PSD could also alter the radiative transfer and heat extraction characteristics within the combustor. In order to understand these mechanisms and identify the optimum operating conditions, fuel particle sizes and fuel (RH/natural gas) mass ratios that minimize the ash deposition, a computational fluid dynamic (CFD) methodology was developed and refined to explain the recent experimental observations of ash deposition and shedding in RH/natural gas combustion scenarios in air and O2/CO2 (70/30 vol %, OXY70) oxidizer compositions. Two different types of RH (US RH and Chinese RH) with widely varying ash contents (by % mass) and inlet fuel PSDs were simulated. With the aid of add-on models for ash deposition, shedding and gas radiative properties, the outer ash deposition and radiative transfer characteristics

were examined. A particle-viscosity- and kinetic-energy (PKE)-based capture criterion was enforced to model the ash capture (following impaction) after identifying appropriate models for RH ash viscosities that were accurate in the temperature region (1200–1300 K) of interest in this study. The energy required to remove a deposited particle was modeled to simulate the shedding behavior. Based on the results of the calculations, the following conclusions were drawn:

1. The predicted temperature profiles along the combustor and particularly near the deposit probe agreed well with the measurements across the four scenarios, demonstrating the adequacy of our combustion modeling procedure. Concurring with experimental observations involving the combustion of several different fuels within this combustor, the simulations also showed that complete carbon burnout occurred prior to the ash deposition at the probe. In spite of the higher oxidizer content in the OXY70 scenario, the gas temperatures near the probe ranged from 1250–1350 K, which is characteristic of gas temperatures near the super heater region in full-scale boilers. Furthermore, the OXY70 scenarios were associated with a 60–70% reduction in the volumetric flow rates. Therefore, the results from this study may provide valuable insights into ash deposition characteristics under load-following operational scenarios (e.g., 35–50% of the base load) where lower velocities but approximately similar temperatures to that of the base load may be encountered.

2. A shrinking core modeling methodology, where the PSD stays invariant from that of the parent fuel throughout the combustion process, and a shrinking sphere methodology, where the density is held constant while the PSD varies, were adopted to assess the particle impacts on the radiation and heat extraction characteristics. Despite the wide PSD variation between the two fuels and the two methodologies, gases dominated the radiative transfer in these configurations. Radiation accounted for 80% and 95% of the overall heat transfer in the AIR and OXY70 firing scenarios, respectively.

3. A well-resolved boundary layer grid was employed near the deposit probe to represent the particle impaction characteristics accurately. In spite of the velocities in the OXY70 scenario being 60–70% lower, the ratios of the impaction rates (OXY70/AIR) were in the range of 1.5–2.0-times for the US RH and in the range 1.1–1.3-times for the Chinese RH when employing conventional char combustion methodologies (shrinking core and shrinking sphere). Since identical parent fuel PSDs were employed for both the AIR and OXY70 scenarios, the fly-ash PSDs near the deposit surface would also be identical near the deposit surface (following complete burnout). Therefore, the surprisingly higher impaction rates associated with the OXY70 scenario points to complex flow features near the probe along with the local segregation of larger sized particles.

4. Based on viscosity measurements in similar silica-rich RH ashes, the temperature-dependent viscosity correlations proposed by Senior and Srinivasachar [23] were deemed to be sufficiently accurate to estimate the ash particle viscosity across the temperature range of interest in this study. However, the predicted deposition rates were grossly under-estimated when employing the PKE-critical viscosity-based ash capture criterion in conjunction with conventional char combustion methodologies (shrinking core and shrinking sphere) pointing to either a need for accurate fly-ash PSD information near the probe or a shortcoming of the capture criterion itself.

5. To identify the source of the discrepancy, measured fly-ash PSDs near the deposit surface (that were only available for the Chinese RH) were employed in the calculations. This improved the deposition rate predictions significantly. The predictions improved further when a simple erosion model (that took the PKE and particle surface tension into account) was employed in conjunction with the capture criterion.

6. When more accurate or representative fly-ash PSDs were employed in these scenarios, the impaction rates were similar in both the AIR and OXY70 conditions. However, the OXY70 scenarios showed higher ash-capturing propensities due to the lower PKE. Conversely, higher erosion rates (due to the larger PKE) were predicted in the AIR firing scenarios. Both these effects may help explain the higher deposition rates measured in OXY70 for both RHs.

Nomenclature

A_P	Particle surface area, m^2
d	Diameter, m
E	Energy, J
k	Extinction coefficient, 1/m
PKE	Particle kinetic energy, J
Q	Extinction efficiency
Re	Reynolds number
Stk	Stokes Number
T	Temperature, K
u	Velocity, m/s
V	Particle volume, m^3
Greek Symbols	
γ	Surface tension, N/m
η	Efficiency
ρ	Density, kg/m^3
μ	Viscosity, kg/m-s
Subscripts	
p	Denotes particle

References

1. Wu, J.; Wang, Y.; Han, J.; Li, X.; Yu, D.; Xu, M.; Wendt, J.O.L. Ash Formation and Deposition in Oxy-fuel Combustion of Rice Husk, Coal, and Their Blend with 70% Inlet O_2. *Energy Fuels* **2019**, *34*, 890–899. [CrossRef]
2. Wang, Y.; Wu, J.; Li, X.; Han, J.; Yu, D.; Xu, M.; Wendt, J.O.L. Comparison Study of Ash Partitioning and Deposition Behavior between Two Rice Husk Fuels under a 100 kW Combustor. *Energy Fuels* **2019**, *33*, 11968–11975. [CrossRef]
3. Wang, Y.; Li, X.; Wendt, J.O.L. Ash Aerosol and Deposition Formation Mechanisms during Air/Oxy-combustion of Rice Husks in a 100 kW Combustor. *Energy Fuels* **2018**, *32*, 4391–4398. [CrossRef]
4. Kleinhans, U.; Wieland, C.; Frandsen, F.J.; Spliethoff, H. Ash formation and deposition in coal and biomass fired combustion systems: Progress and challenges in the field of ash particle sticking and rebound behavior. *Prog. Energy Combust. Sci.* **2018**, *68*, 65–168. [CrossRef]
5. Black, S.; Szuhánszki, J.; Pranzitelli, A.; Ma, L.; Stanger, P.J.; Ingham, D.B.; Pourkashanian, M. Effects of firing coal and biomass under oxy-fuel conditions in a power plant boiler using CFD modelling. *Fuel* **2013**, *113*, 780–786. [CrossRef]
6. Seidel, T.; Krishnamoorthy, G.; Seames, W.S. Characterizing flame stability and radiative heat transfer in non-swirling oxy-coal flames using different multiphase modeling frameworks. *Fuel* **2019**, *256*, 115948. [CrossRef]

7.   Andersson, K.; Johansson, R.; Hjärtstam, S.; Johnsson, F.; Leckner, B. Radiation intensity of lignite-fired oxy-fuel flames. *Exp. Therm. Fluid Sci.* **2008**, *33*, 67–76. [CrossRef]

8.   Krishnamoorthy, G.; Sami, M.; Orsino, S.; Perera, A.; Shahnam, M.; Huckaby, E.D. Radiation modelling in oxy-fuel combustion scenarios. *Int. J. Comput. Fluid Dyn.* **2010**, *24*, 69–82. [CrossRef]

9.   Nakod, P.; Krishnamoorthy, G.; Sami, M.; Orsino, S. A comparative evaluation of gray and non-gray radiation modeling strategies in oxy-coal combustion simulations. *Appl. Therm. Eng.* **2013**, *54*, 422–432. [CrossRef]

10. Krishnamoorthy, G.; Wolf, C. Assessing the Role of Particles in Radiative Heat Transfer during Oxy-Combustion of Coal and Biomass Blends. *J. Combust.* **2015**, *2015*, 1–15. [CrossRef]

11. Zhang, J.; Ito, T.; Ito, S.; Riechelmann, D.; Fujimori, T. Numerical investigation of oxy-coal combustion in a large-scale furnace: Non-gray effect of gas and role of particle radiation. *Fuel* **2015**, *139*, 87–93. [CrossRef]

12. Yang, X.; Clements, A.; Szuhánszki, J.; Huang, X.; Moguel, O.F.; Li, J.; Gibbins, J.; Liu, Z.; Zheng, C.; Ingham, D.; et al. Prediction of the radiative heat transfer in small and large scale oxy-coal furnaces. *Appl. Energy* **2018**, *211*, 523–537. [CrossRef]

13. Adams, B.R.; Hosler, T.R. Pressure and particle property impacts on radiation in oxy-coal combustion. *Fuel* **2019**, *239*, 667–676. [CrossRef]

14. Kez, V.; Consalvi, J.-L.; Liu, F.; Gronarz, T.; Ströhle, J.; Kneer, R.; Epple, B. Investigation of gas and particle radiation modelling in wet oxy-coal combustion atmospheres. *Int. J. Heat Mass Transf.* **2019**, *133*, 1026–1040. [CrossRef]

15. Guo, J.; Hu, F.; Jiang, X.; Li, P.; Liu, Z. Effects of gas and particle radiation on IFRF 2.5 MW swirling flame under oxy-fuel combustion. *Fuel* **2019**, *263*, 116634. [CrossRef]

16. Johansson, R.; Gronarz, T.; Kneer, R. Influence of Index of Refraction and Particle Size Distribution on Radiative Heat Transfer in a Pulverized Coal Combustion Furnace. *J. Heat Transf.* **2017**, *139*, 042702. [CrossRef]

17. Chaloupková, V.; Ivanova, T.; Hutla, P.; Špunarová, M. Ash melting behavior of rice straw and calcium additives. *Agriculture* **2021**, *11*, 1282. [CrossRef]

18. Atallah, E.; Defoort, F.; Pisch, A.; Dupont, C. Thermodynamic equilibrium approach to predict the inorganic interactions of ash from biomass and their mixtures: A critical assessment. *Fuel Process. Technol.* **2022**, *235*, 107369. [CrossRef]

19. Schulze, K.; Hofmeister, G.; Joeller, M.; Scharler, R.; Obernberger, I.; Korbee, R.; Cieplik, M. Development and evaluation of a flexible model for CFD simulation of ash deposit formation in biomass fired boilers. In Proceedings of the International Conference "Impacts of Fuel Quality on Power Production", EPRI Report (No. 1014551), Snowbird, UT, USA, 29 October–3 November 2007; pp. 7–95.

20. Krishnamoorthy, G. A new weighted-sum-of-gray-gases model for oxy-combustion scenarios. *Int. J. Energy Res.* **2013**, *37*, 1752–1763. [CrossRef]

21. Krishnamoorthy, G. Aerodynamic influences on the outer ash deposition rates during oxy-coal combustion. *Clean. Chem. Eng.* **2022**, *3*, 100057. [CrossRef]

22. Krishnamoorthy, G.; Kuznia, M.E.; Smith, K.M.; Seames, W.S.; Wang, Y.; Wendt, J.O. Aerodynamic effects on outer ash deposition rates in second generation atmospheric pressure oxy-coal combustion systems. *Fuel* **2021**, *303*, 121217. [CrossRef]

23. Senior, C.L.; Srinivasachar, S. Viscosity of Ash Particles in Combustion Systems for Prediction of Particle Sticking. *Energy Fuels* **1995**, *9*, 277–283. [CrossRef]

24. Zhou, H.; Zhang, H.; Li, L.; Zhou, B. Ash Deposit Shedding during Co-combustion of Coal and Rice Hull Using a Digital Image Technique in a Pilot-Scale Furnace. *Energy Fuels* **2013**, *27*, 7126–7137. [CrossRef]

25. Dizaji, H.B.; Zeng, T.; Hölzig, H.; Bauer, J.; Klöß, G.; Enke, D. Ash transformation mechanism during combustion of rice husk and rice straw. *Fuel* **2022**, *307*, 121768. [CrossRef]

26. Krishnamoorthy, G. Modeling Ash Deposition and Shedding during Oxy-Combustion of Coal/Rice Husk Blends at 70% Inlet O_2. *Int. J. Coal Sci. Technol.* **2023**. *accepted*. [CrossRef]

27. Weber, R.; Schaffel-Mancini, N.; Mancini, M.; Kupka, T. Fly ash deposition modelling: Requirements for accurate predictions of particle impaction on tubes using RANS-based computational fluid dynamics. *Fuel* **2013**, *108*, 586–596. [CrossRef]

28. ANSYS, Inc. *ANSYS Fluent Theory Guide*; Release 21.1; ANSYS, Inc.: Canonsburg, PA, USA, 2021.

29. Bäckström, D.; Gall, D.; Pushp, M.; Johansson, R.; Andersson, K.; Pettersson, J.B. Particle composition and size distribution in coal flames–The influence on radiative heat transfer. *Exp. Therm. Fluid Sci.* **2015**, *64*, 70–80. [CrossRef]

30. Ates, C.; Selçuk, N.; Kulah, G. Influence of fly ash composition on non-gray particle radiation in combusting systems. *J. Quant. Spectrosc. Radiat. Transf.* **2018**, *215*, 25–40. [CrossRef]

31. Jiayu, L.; Xiaobing, G. Influence of Particle Morphology on High-Temperature Heat Flux to Combustor Walls. *J. Thermophys. Heat Transf.* **2019**, *33*, 574–579. [CrossRef]

32. Schiemann, M.; Gronarz, T.; Graeser, P.; Gorewoda, J.; Kneer, R.; Scherer, V. A correlation between char emissivity and temperature. *Fuel* **2019**, *256*, 115889. [CrossRef]

33. Pörtner, L.; Gu, Y.; Schiemann, M. Investigation of Pulverized Biomass and Coal Char Emissivity. *Energies* **2020**, *13*, 4620. [CrossRef]

34. Doner, N.; Topal, H.; Aygahoglu, A.; Sen, F.; Karimi-Maleh, H. Study on particle radiative properties of lignite, hard coal and biomass fly ashes in the infrared wavelength range. *Chemosphere* **2021**, *291*, 132719. [CrossRef]

35. Zhou, H.; Hu, S. Numerical simulation of ash deposition behavior with a novel erosion model using dynamic mesh. *Fuel* **2020**, *286*, 119482. [CrossRef]